aerospace

MDPI

Article

Configuration Design and Dynamic Characteristics Analysis for Space Membrane Mechanism Based on Deployable Booms

Yuzhen Tang [1,*], Hongwei Guo [1], Wenyao Zhang [1], Zhiyi Wang [2], Chao Xie [2] and Rongqiang Liu [1]

[1] State Key Laboratory of Robotics and System, Harbin Institute of Technology, Harbin 150001, China
[2] Space Structure and Mechanism Technology Laboratory of China Aerospace Science and Technology Group Co., Ltd., Shanghai 201108, China
[*] Correspondence: tangyuzhen@hit.edu.cn

Abstract: To meet the requirements of deployable structures in aerospace engineering with light weight and high stiffness, this paper proposes the triangular space membrane deployable mechanism based on deployable booms, then conducts dynamic analysis and multiobjective optimization. The configuration design and mass calculation for the membrane mechanism are carried out, including its unfolding support mechanism and tensioned membrane scheme. With a view to performing the dynamic characteristics analysis and parametric studies, the finite element simulation model of the membrane mechanism, including boom, cable and membrane, is built and validated against test results obtained by Polytec. On the basis of the simulation results, a surrogate model of fundamental frequency is established by adopting the response surface method and applied to multiobjective optimization combined with the mass formula. Then, the optimal dynamic and lightweight design parameters are solved via the genetic algorithm. The results provide an indication to aid with the design and analysis of space membrane deployable mechanisms according to the required properties and space mission requirements.

Keywords: space membrane deployable mechanism; configuration design; dynamic analysis; deployable boom; tensioned membrane; response surface method

check for updates

Citation: Tang, Y.; Guo, H.; Zhang, W.; Wang, Z.; Xie, C.; Liu, R. Configuration Design and Dynamic Characteristics Analysis for Space Membrane Mechanism Based on Deployable Booms. *Aerospace* **2023**, *10*, 239. https://doi.org/10.3390/aerospace10030239

Academic Editor: Pierre Rochus

Received: 9 November 2022
Revised: 21 February 2023
Accepted: 26 February 2023
Published: 1 March 2023

1. Introduction

With the increasingly urgent demand for large-scale antennas, solar panels, solar sails and other space structures, the research on deployable mechanisms has started to gather attention in recent years [1,2]. Compared with the traditional rigid deployable mechanisms, space membrane deployable mechanisms with significant advantages in system quality and deployment ratio are becoming a creative approach for specific space applications [3].

Extensive research on space membrane deployable mechanisms has yielded a large number of remarkable engineering applications, ranging from space membrane antennas [4,5] and membrane solar cell arrays [6,7] to large-area solar sails [8–10]. With an increasing demand for high-resolution Earth observation [11], innovative large-scale deployable membranes antenna have recently been attracting significant interest. The DLR and European Space Agency (ESA) collaborated to develop the deployable Synthetic Aperture Radar (SAR) antenna composed of membranes and two coilable booms [12]. Due to the advantages of areal density and power-to-mass ratio, the Hubble solar array jointly developed by the National Aeronautics and Space Administration (NASA) and ESA [13], the International Space Station (ISS) solar array [14] and Roll Out solar array (ROSA) [15,16] all adopted membrane solar cell arrays. In the Interplanetary Kite-craft Accelerated by Radiation Of the Sun (IKAROS) solar sail [17] and Nanosail-D [18] solar sail, which have been successfully launched, deployed and carried out in-orbit tests, membrane deployable mechanisms are necessary for deep space exploration. The implementation of membrane in these typical large-scale space structures indicates that the membrane deployable mechanism is the key development field in both engineering and academia.

Despite light weight, large deployment ratio and low cost, the dynamic problems of the membrane deployable mechanism are inevitable and prominent considering the large flexibility of the membrane and complexity of the space environment [19]. As discussed above, many efforts have been made by scholars on dynamic characteristics [20] and experimental analysis [21]. Shen et al. [22] of the Canadian Space Agency (CSA) established membrane models in simulation software and analyzed the effect of tension forces and damping ratios. The assumed mode method was adopted to conduct membrane analysis by Liu et al. [23,24] and compared with nonlinear finite method, which indicated that the former result is smaller. Using the coupling coefficient approach, Fan et al. [25] studied the coupling dynamics characteristics of a satellite and membrane. Ahmadi et al. [26] investigated the effects of different parameters on the frequency ratio and nonlinear frequency of a prestressed membrane. As previously stated, numerous discussions have focused on the analysis and modeling of single membranes, while the dynamic characteristics of the boom–cable–membrane coupling overall system have been considered in little research so far. Many researchers have examined noncontact membrane measurement due to the delicate and flexible properties of membranes. Both Zhang et al. [27] and Chakravarty et al. [28] adopted laser Doppler vibrometers (LDV) to conduct noncontact vibration tests to measure the membranes, respectively. Moreover, the tie-system calibration [29] can provide an indication to the experimental setup for the tensioning of membranes. A novel, nondestructive methodology, using vibro-acoustic tests to measure the membrane modal characteristics and mechanical properties was put forward by Lima-Rodriguez et al. [30] recently. Gaspar et al. [31] from NASA conducted a noncontact modal test of membranes using the Polytec scanning laser vibrometer and discussed the results obtained at various tension levels and at various excitation locations.

In order to address the conflict between the large scale required of the deployed space membranes and the performance of high stiffness, the configuration design and multiobjective optimization can provide solutions. As for the configuration design, the deployable booms and web-like tensioned membrane scheme are major prerequisites for the implementation of high-stiffness, lightweight design. Deployable membranes coupled with booms have been extensively studied, ranging from Synthetic Aperture Radar (SAR) satellite [32] and deployable membrane structures with rolled-up booms [33,34] to 3U CubeSat OrigamiSat-1 [35], which focus on conceptual model design and on-orbit experiments. However, little research has derived the mass equation based on the analysis of the cable tension theoretically. The studies on deployable membranes using the multiobjective optimization approach [36,37] can provide an indication to tune parameters for the membrane mechanism designed in this work. By the response surface method, the dynamic surrogate model based on the boom–cable–membrane mechanism simulation results is established, and then combined with the derived mass equation to conduct multiobjective optimization, which has been considered in little of the research on overall deployable membrane systems compared with single-component ones so far. In this work, the aim is to explore the configuration design process, including deployable booms and tensioned schemes and multiobjective optimization based on a mathematical surrogate model to produce a deployable membrane mechanism with satisfactory dynamic performance of weight and stiffness.

In Section 2, the configuration design and analysis of a space membrane deployable mechanism, as well as mass calculation for deployable booms, membranes and cables, respectively, are presented. The boom–cable–membrane dynamic simulation model is given in Section 3 and verified by the modal test of scaled prototype. Section 4 provides surrogate model establishment of the fundamental frequency and its application to multiobjective optimization with the mass formula.

2. Configuration Design and Mass Calculation for Space Membrane Deployable Mechanism

To meet the requirements of the properties for deployable structures in aerospace engineering, including light weight, high deployment ratio, high stiffness and large size, the triangular space membrane deployable mechanism based on deployable booms is proposed, as shown in Figure 1. This mechanism with height h consisting of an unfolding support mechanism, a membrane and a tensioning system, has the advantages of excellent deployment synchronization and ease of control, fewer deployment units and lower surface density. The membrane is folded according to Miura-ori, and the deployable booms are wrapped into the folded state. During deployment, the deployable booms drive the cables, and the cables drive the membrane to unfold and be tensioned by the web-like tensioned membrane scheme.

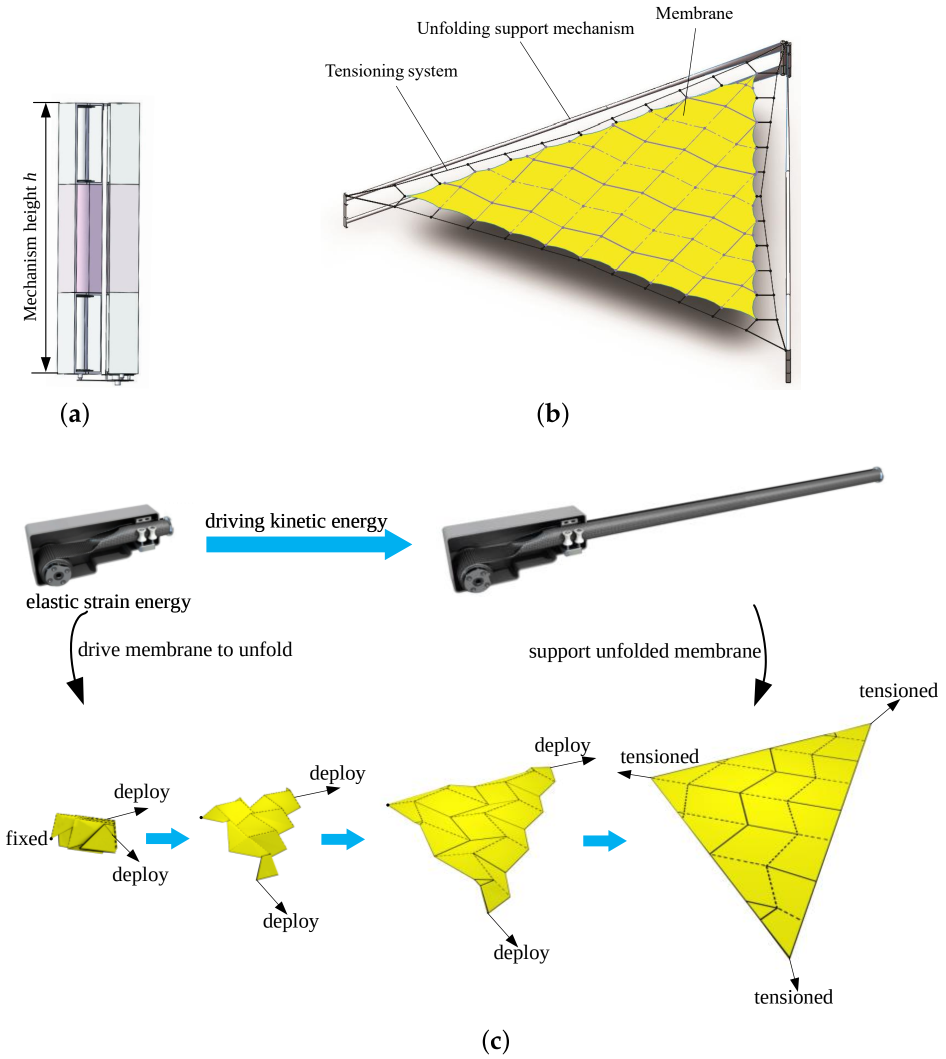

Figure 1. (**a**) Folded state of the triangular space membrane deployable mechanism. (**b**) Unfolded state of the triangular space membrane deployable mechanism. (**c**) Schematic of the mechanism in action during deployment of the membrane.

2.1. Unfolding Support Mechanism

Compared with the rigid truss, the deployable boom is utilized as the unfolding support mechanism for the triangular space membrane deployable mechanism because of its light weight, high deployment ratio and self-deployable performance, and the prerequisites for the same stowed height and mass are set when selecting sections. As shown in Figure 2, there are mainly three different sections of deployable booms: the storable tubular extendable member (STEM), the collapsible tube mast (CTM) and the triangular rollable and collapsible (TRAC) boom (orient 90°), so that these three sections are symmetric with respect to the y-axis of the established local coordinate system.

Then, the flexural stiffness EI_x and principal moment of inertia I_x of the deployable booms can be calculated analytically according to the inertia moment, the static moment and the formula of parallel displacement axis, and the STEM is taken as an example to illustrate the calculation procedure, as shown in Equation (1). As for the unfolding support mechanism, the flexural stiffness of these three sections is calculated and compared in the case of the same stowed height and mass M_{db}, which can provide guidance on the section selection.

$$\begin{cases} I_{x_1} = \iint_A y^2 dA = 2\int_{-\frac{\pi}{2}}^{\frac{\pi}{2}-\theta_1} R^2 \sin^2\theta d\theta \int_{r-\delta}^{r} RdR \\ d = \frac{S_{x_1}}{A} = \frac{\iint_A ydA}{A} = \frac{2\int_{r-\delta}^{r} RdR \int_{-\frac{\pi}{2}}^{\frac{\pi}{2}-\theta_1} R\sin\theta d\theta}{A} \\ I_{x_2} = I_{x_1} - d^2 A \end{cases} \quad (1)$$

where A represents the cross-sectional area, and the parametric equation for the cross-section curve is $x^2 + y^2 = R^2$.

Since the Young's modulus E of the three sections of booms is the same, the principal moment of inertia I_x can be selected to compare the flexural stiffness and assess the sections. The deployable booms are made of carbon fiber with a Young's modulus of 96 GPa and a density of 1600 kg/m^3. Addiitonally, the geometric parameters of the booms are of length L = 31.25 m, b_c = 96 mm and b_t = 220 mm, radius r = 110 mm and r_t = 275 mm, opening angle $\theta = 20°$ and boom thickness $\delta = 0.5$ mm. According to these material and geometric parameters, the calculation results of the three sections can be obtained.

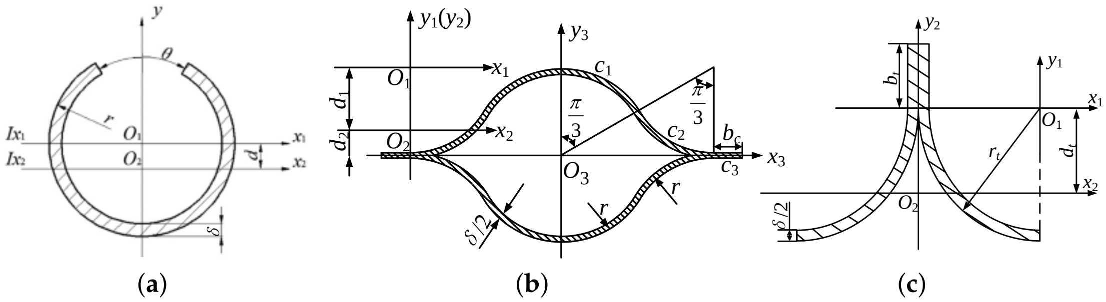

Figure 2. Three sections of deployable booms: (**a**) STEM. (**b**) CTM. (**c**) TRAC (orient 90°).

It can be seen from the results listed in Table 1 that the CTM is a closed-loop cross-section with the smallest inertia. On the precision of the same mass, the TRAC has the largest inertia, but its performance is seriously affected by the machining accuracy, especially the strict bonding requirements.However, the STEM is an integral structure with higher reliability than other forms, is made from a pair of symmetric halves bonded at the edges and has relatively balanced mechanical properties in all directions. Therefore, the STEM is selected as the cross-sections of the deployable booms applied to the triangular space membrane deployable mechanism because of its better properties and ease of manufacture.

Table 1. Calculation results of three sections.

Cross-Section	Inertia I_x (mm^4)	Mass M_{db} (kg)
STEM	1.85×10^6	16.27
CTM	1.06×10^6	16.27
TRAC	2.29×10^6	16.27

2.2. Tensioned Membrane Scheme

In view of the large-size triangular membrane structure, five kinds of tensioned membrane schemes in Figure 3 are designed, respectively, they are the corner tensioning scheme, conventional catenary design, Miura–Natori tensioning system, shear-compliant border design and the web-like tensioned membrane scheme, varying in the boundary shape of the membranes and the arrangement of the catenaries. The web-like tensioned membrane scheme is selected considering that it effectively reduces the overall mass of the cables and improves the surface accuracy and flatness of the membrane by greatly eliminating wrinkles. The outer perimeter cables can be used to absorb the majority of disturbances emanating from the support points, alleviating the membrane wrinkles as a result.

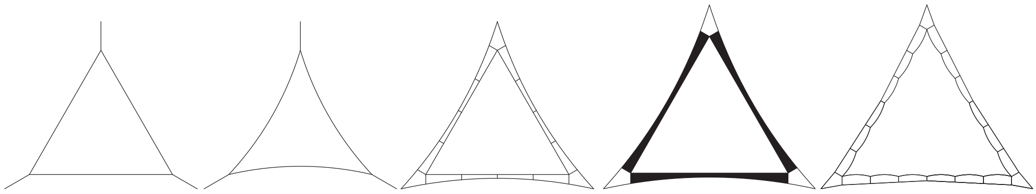

Figure 3. Five kinds of tensioned membrane schemes.

The membrane is attached to the inner catenary cables across the three curved edges of the triangle, and the inner catenary and outer perimeter cables are coupled by tie cables, as denoted in Figure 4. Each triangular edge consists of N arcs with radius of r_{wg}, then r_{wg} can be deduced according to the geometric relations illustrated in Figure 4, as shown in Equation (2),

$$r_{wg} = \frac{l}{N} \frac{1}{2 \sin \theta_{wg}/2} \quad (2)$$

where the side length of the membrane l and the angle θ_{wg} are labeled in Figure 4.

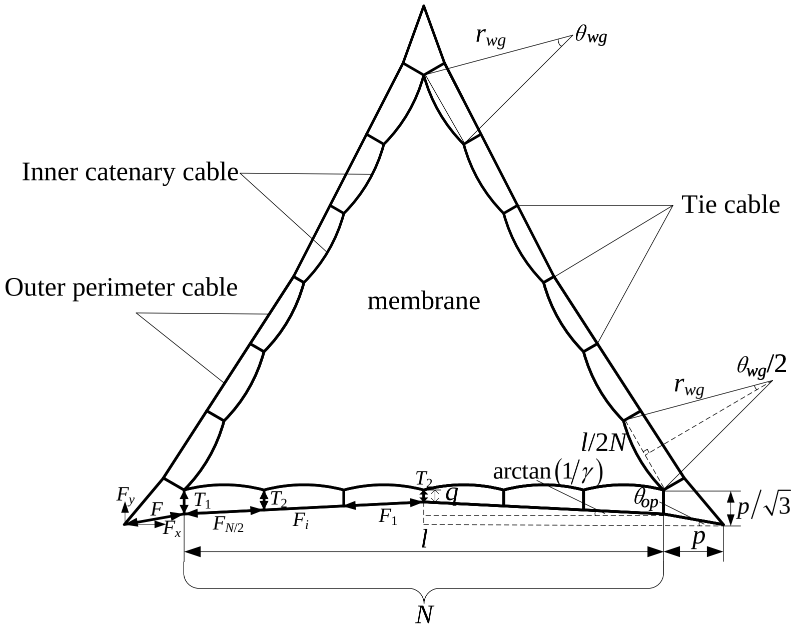

Figure 4. Web-like tensioned membrane scheme.

As plotted in Figure 5, one arc of the inner catenary cable and part of the membrane are extracted from the web-like tensioned membrane scheme. According to the equilibrium condition, the uniform tension in inner catenary cable T_{ic} is given as

$$T_{ic} = r_{wg}\sigma_m \quad (3)$$

where σ_m is the membrane uniform stress. Moreover, T_{ic} is expressed as

$$T_{ic} = E_{ic}A_{ic}\varepsilon_{ic} \quad (4)$$

where E_{ic}, A_{ic} and ε_{ic} represent the Young's modulus, the cross-sectional area and the uniform strain of the inner catenary cables, respectively. The membrane uniform stress σ_m is assumed to be constant, and can be calculated as

$$\sigma_m = \frac{E_m t}{1 - v} \varepsilon_m \tag{5}$$

where E_m, t, v and ε_m represent Young's modulus, thickness, Poisson's ratio and uniform strain of the membrane, respectively.

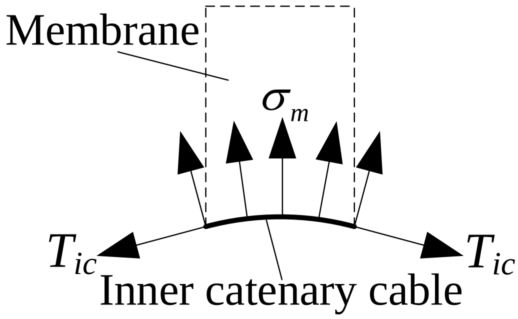

Figure 5. Extraction diagram of web-like tensioned membrane scheme.

With the assumption that the membrane wrinkle is negligible, ε_{ic} is considered equal to ε_m. Then, substituting Equations (2), (4) and (5) to Equation (3), A_{ic} is analytically derived based on the equations above as

$$A_{ic} = \frac{l E_m t}{2N E_{ic} (1 - v) \sin \theta_{wg}/2} \tag{6}$$

Combined with the geometric relations, the total length of the inner catenary cables l_{ic} is expressed as follows:

$$l_{ic} = 3N r_{wg} \theta_{wg} \tag{7}$$

As shown in Figure 4, T_1 and T_2 represent the tensions in tie cables. According to the equilibrium condition and Equation (4), T_1 and T_2 can be expressed as

$$\begin{cases} T_1 = 2\cos\left(\frac{\pi}{6} - \frac{\theta_{wg}}{2}\right) E_{ic} A_{ic} \varepsilon_{ic} \\ T_2 = 2\sin\frac{\theta_{wg}}{2} E_{ic} A_{ic} \varepsilon_{ic} \end{cases} \tag{8}$$

Considering equilibrium, the tensions in outer perimeter cables F_i $(i = 1, 2, \ldots, N/2)$ labeled in Figure 4 can be obtained as

$$\begin{cases} F_{ix} = \frac{\gamma}{2} T_2 \quad (i = 1, 2, \ldots, N/2) \\ F_{iy} = \frac{2i-1}{2} T_2 \end{cases} \tag{9}$$

where $\frac{1}{\gamma}$ describes the gradient and is given as

$$\frac{1}{\gamma} = \frac{dy}{dx} = \frac{p/\sqrt{3} - q - p\tan\theta_{op}}{l/2} \tag{10}$$

in which $\theta_{op} = \arctan(F_y/F_x)$, and the relevant parameters are annotated in Figure 4. Combined with Equation (9) and equilibrium, the cable tension F can be obtained as

$$\begin{aligned} F &= \sqrt{{F_x}^2 + {F_y}^2} \\ &= T_2 \sqrt{\frac{\gamma^2}{4} + \left(\frac{T_1}{T_2} + \frac{N-1}{2}\right)^2} \end{aligned} \tag{11}$$

From Equation (11), the following equation can be calculated.

$$\tan\theta_{op} = \left(\frac{T_1}{T_2} + \frac{N-1}{2}\right) / \frac{\gamma}{2} \tag{12}$$

Substituting Equation (12) into Equation (10), the final expression of $\frac{1}{\gamma}$ can be obtained as

$$\frac{1}{\gamma} = \frac{\frac{1}{2}(p/\sqrt{3} - q)}{\frac{l}{4} + \left(\frac{T_1}{T_2} + \frac{N-1}{2}\right)p} \tag{13}$$

and then the total length of the tie cables l_{tie} and outer perimeter cables l_{oc} can be obtained, respectively, as follows:

$$\begin{cases} l_{tie} = \frac{3(N+2)}{4\gamma} l + 3(N+1)q \\ l_{oc} = 6p\sqrt{\frac{\gamma^2}{4} + \left(\frac{T_1}{T_2} + \frac{N-1}{2}\right)^2} + \frac{3l\sqrt{\gamma^2+1}}{\gamma} \end{cases} \tag{14}$$

Similar to Equation (4), F can also be expressed as

$$F = E_{oc} A_{oc} \varepsilon_{oc} \tag{15}$$

where E_{oc} and ε_{oc} are Young's modulus and the uniform strain of the outer perimeter cables. The cross-sectional area of the outer perimeter cables A_{oc} is assumed equal to that of the tie cables A_{tie}. Based on the derivations above, when the material properties of the cables and membrane and these geometric parameters, including l, p, q, θ_{wg}, ε_{oc} and N, are given, the total length of all the cables l_{ic}, l_{tie} and l_{oc} can be calculated, respectively, and the cross-sectional area of various cables are simplified as a function of F and t. Then, the total length and cross-sectional area of the cables are substituted into the mass calculation and the multiobjective optimization of subsequent sections. Meanwhile, these derivations also guide the design of the tensioned scheme applied in the FEA model by calculating the variables, such as r_{wg} and $\frac{1}{\gamma}$.

2.3. Mass Calculation

As mentioned above, the membrane mechanism consists of STEM deployable booms, tensioned cables and membrane, and the total mass equation based on the cross-sectional areas and the total length of the cables gained above is derived here to establish the analytical model on design parameters, which is applied to the multiobjective optimization in a subsequent section. Consequently, a total mass equation can be established:

$$M = M_b + M_c + M_m \tag{16}$$

where M_c represents the mass of the web-like cables, and the mass of the STEM deployable booms M_b = 32.54 kg, as listed in Table 1. The mass of the membrane M_m is derived as follows:

$$M_m = \rho_m \left[\frac{\sqrt{3}}{4} l^2 - \frac{3N r_{wg}^2}{2}\left(\theta_{wg} - \sin\theta_{wg}\right)\right] t \tag{17}$$

where ρ_m represents the density of the membrane. Moreover, the total mass of cables M_c is given by

$$M_c = \rho_c A_{ic} l_{ic} + \rho_c A_{oc}(l_{tie} + l_{oc}) \tag{18}$$

where ρ_c is the density of the cables. The material of the membrane is Kapton with density of 1420 kg/m^3, Young's modulus of 2.5 GPa and Poisson's ratio of 0.34. Additionally, the cables are Kevlar with a density of 1440 kg/m^3, Young's modulus of 131GPa and Poisson's ratio of 0.35. Furthermore, other geometric parameters are l = 25 m, $p = l/8$, $q = l/100$, $\theta_{wg} = 30°$, $\varepsilon_{oc} = 0.1\%$ and N = 10. According to these material and geometric parameters, the total mass of all the cables M_c is only related to the cable tension F and the membrane thickness t by substituting Equations (6), (7), (14) and (15) into Equation (18), as shown in the following equation.

$$M_c = 0.0013F + 0.015t \tag{19}$$

Substituting the parameters mentioned above into Equation (17), M_m can be obtained as

$$M_m = 0.373t \tag{20}$$

In summary, Equation (16) can be rewritten as

$$M = 0.0013F + 0.388t + 32.54 \tag{21}$$

3. Dynamic Analysis of Space Membrane Deployable Mechanism

3.1. Finite Element Model

In simulation software ANSYS, the FE model of space membrane deployable mechanisms, including booms, cables and membrane, is established based on the aforementioned configuration design, as shown in Figure 6. The geometric parameters and material properties of the membrane mechanism are consistent with those mentioned in the previous section, and the latter is summarized and listed in Table 2.

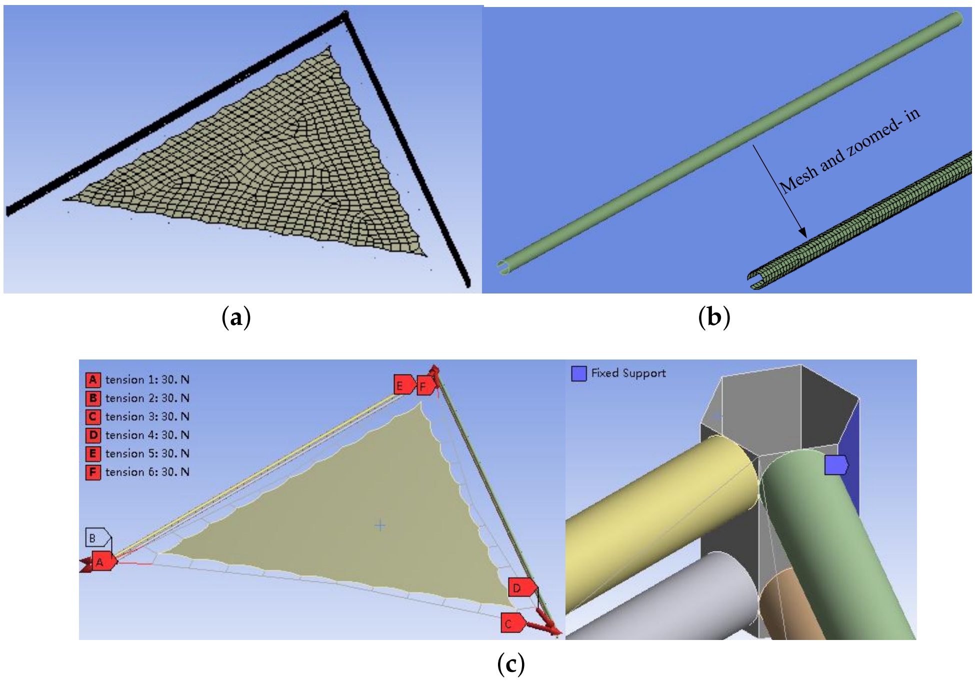

Figure 6. (**a**) FE model of space membrane deployable mechanism. (**b**) Zoomed-in view of the STEM. (**c**) Tensions and fixed support.

Table 2. Material properties.

Material Properties	Carbon Fiber	Kapton	Kevlar
ρ (kg/m^3)	1600	1420	1440
E (GPa)	96	2.5	131
v	0.3	0.34	0.35

Thus, there are four unspecified parameters, respectively: mechanism height h, cable tension F, boom thickness δ and membrane thickness t, the parametric studies of which are carried out in the subsequent section. Here, only the case of h = 0.6 m, F = 30 N, δ = 0.50 mm and t = 25 µm is taken as an example to illustrate the FE modeling method. In the simulation, the membrane is modeled with Shell181 element, the booms are modeled with Beam 188 element and various cables are modeled with Link10 element. Considering the mesh convergence and simulation accuracy, a mesh of 9409 elements is adopted to model the whole mechanism. Bonded contact is adopted to model the attachment between the booms, cables and membrane. The root of the deployable booms is a fixed constraint, and the cable tension of 30 N is applied to the cables, as depicted in Figure 6c. Thus, the mode shape and frequency of the membrane mechanism can be analyzed, and the results are illustrated in Figure 7 with a fundamental frequency of 0.1302 Hz.

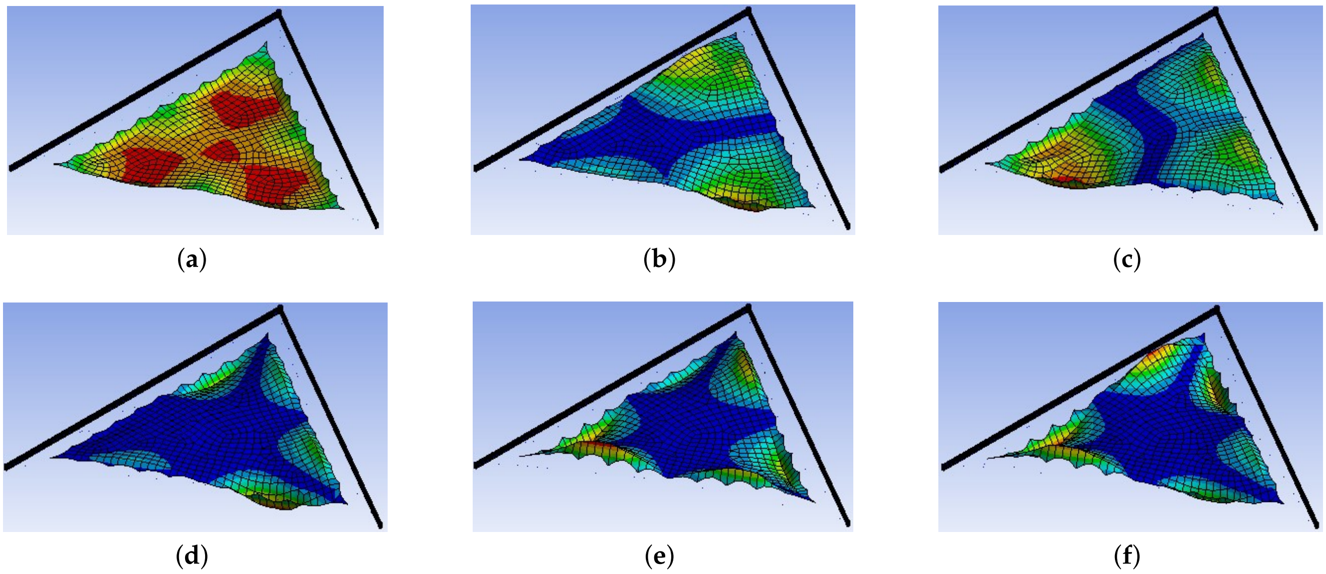

Figure 7. The first 6-order mode shapes: (**a**) 1st, (**b**) 2nd, (**c**) 3rd, (**d**) 4th, (**e**) 5th and (**f**) 6th.

3.2. Model Test Verification

To achieve noncontact measurement, the Polytec laser vibrometer is selected to measure the mode shape and frequency of the model membrane mechanism by scanning it with the laser camera, as shown in Figure 8. During the test, the Polytec controller controls the vibrator through the power amplifier to provide controllable excitation for the test frame, which drives the membrane mechanism vibration. After the vibration speed information of each target of the membrane mechanism is collected by the laser camera, the final test results are obtained by the Polytec postprocessing system. To keep consistent with the boundary conditions in the simulation, the root of the deployable booms is fixed on the test frame and the membrane surface is facing the laser camera to offload the gravity. The outer perimeter cables are connected to the boom ends directly to support the membrane, and the cable tensions are applied by adjusting the length of the cables and measured by the tension meter, as shown in Figure 8.

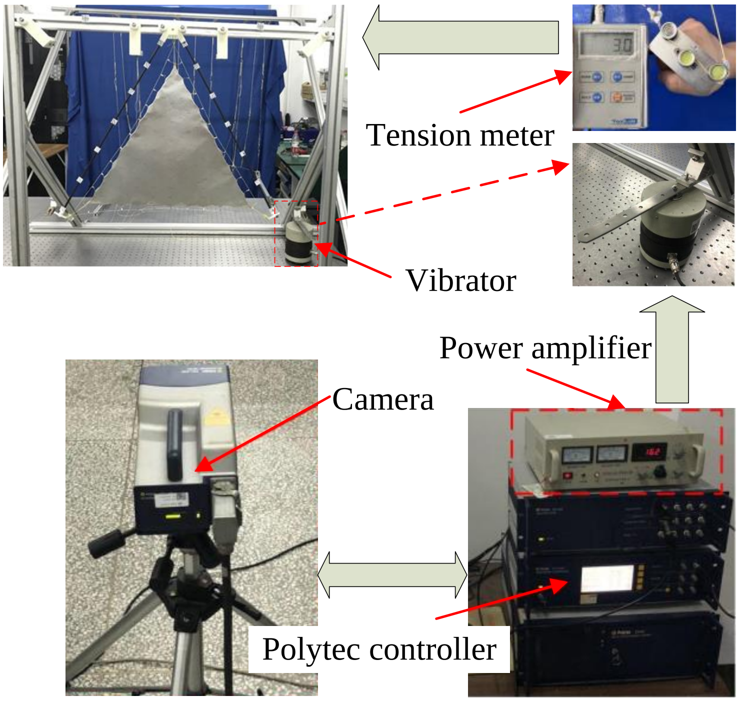

Figure 8. Modal test of membrane mechanism.

Due to the limited experimental condition, the scaled prototype of the membrane mechanism with a side length of 0.5 m is taken as test object. In order to verify more accurately, a new finite element model of the scaled prototype is built using the same modeling method and simulation settings as in the previous section and applied with the cable tension of 3 N. Hence, the validation is conducted by comparing the mode shapes in Figure 9 and frequencies listed in Table 3. It can be seen from Figure 9 that the low-order vibration modes of both the test and simulation results are all out-plane vibration modes, and the vibration of the membrane and cables play the major role. Compared with the booms, the membrane and the cables are more flexible, so in the vibration analysis, the location of deformation is mainly found at the membrane and cables due to torsional and bending vibration. Additionally, in the model test, the booms also do not have a large displacement when the vibrator provides controllable excitation, mainly because of the stiffness difference. The vibration of booms in the boom–cable–membrane system would play a great role in enlightening our future research, especially the relationship between the vibration results of the boom, cable and membrane by analytical model with reference to relevant theories, a more accurate simulation model and more advanced test equipment. The first three simulation mode shapes correspond basically with the test mode shapes, and the differences are mainly because the Polytec vibrometer uses interpolation calculation in data processing. The accuracy of the simulation and test would be further improved in subsequent research. Additionally, the simulation frequencies ω_{FE} are somewhat lower than the test frequencies ω_{test}, which are all within the acceptable range. This demonstrates the correctness of the finite element model of the boom–cable–membrane mechanism.

Table 3. Comparison between ω_{FE} and ω_{test}.

Order	ω_{FE} (Hz)	ω_{test} (Hz)	Error
1st	3.34	3.5	4.6%
2nd	5.82	6.25	6.9%
3rd	6.28	7	10.3%

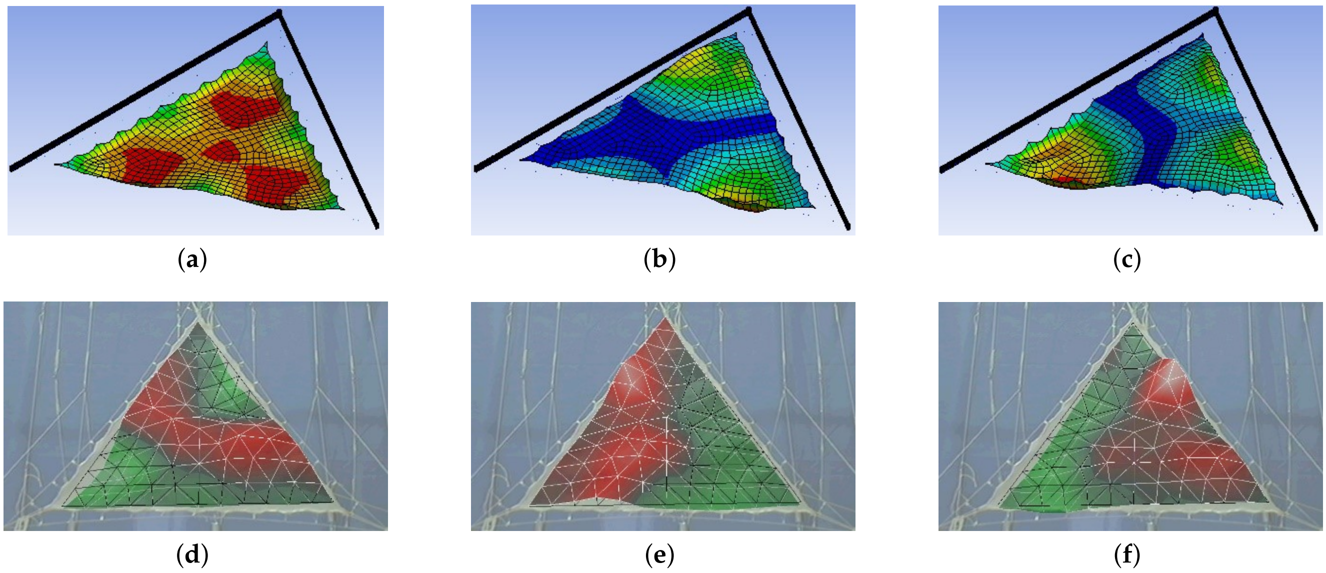

Figure 9. Comparison between test and simulation mode shapes: (**a**) 1st simulation mode, (**b**) 2nd simulation mode, (**c**) 3rd simulation mode, (**d**) 1st test mode, (**e**) 2nd test mode and (**f**) 3rd test mode.

3.3. Parametric Studies

The influence law of parameters, including mechanism height h, cable tension F, boom thickness δ and membrane thickness t, is studied, as shown in Figure 10. In the process of analyzing any one parameter, the other three parameters should be kept fixed. It can be seen that within the given range shown in the figures, both the increase in cable tension and boom thickness could cause the fundamental frequency to increase, while the fundamental frequency decreases as the membrane thickness increases. Additionally, the fundamental frequency ω rapidly increases with the increase in mechanism height, but the initial trend slows and then decreases. From the figures, it can be inferred that the fundamental frequency is more sensitive to the cable tension and the membrane thickness, because when the cable tension F changes from 30 N to 40 N, ω increases by 14.29%, and when the membrane thickness t changes from 25 µm to 125 µm, ω decreases by 54.95%. As the mode shapes mentioned above can also illustrate that the location of deformation is mainly found at the membrane and cables due to torsional and bending vibration, the cable tension and the membrane thickness of these two parameters possess more pronounced impact on the fundamental frequency.

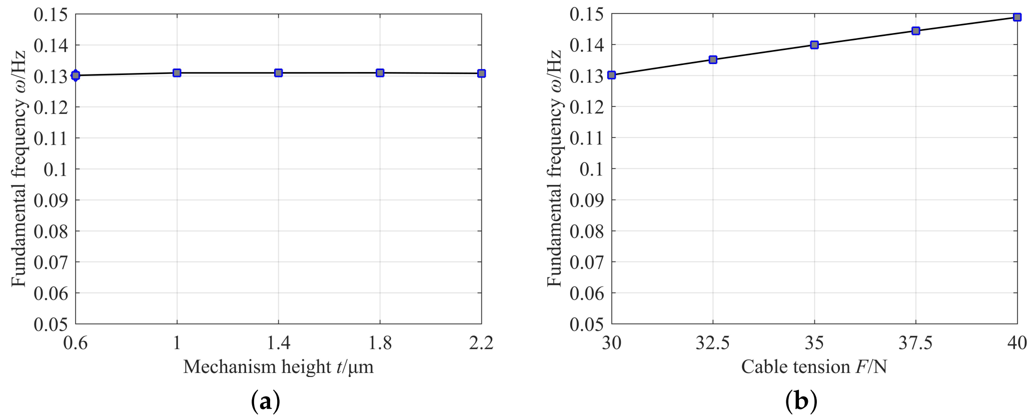

Figure 10. *Cont.*

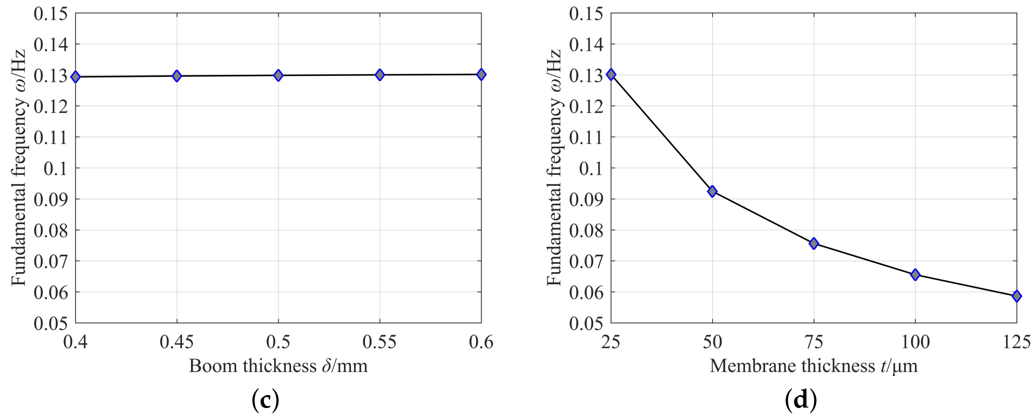

Figure 10. Effect of parameters: (**a**) effect of mechanism height, (**b**) effect of cable tension, (**c**) effect of boom thickness and (**d**) effect of membrane thickness.

4. Response Surface Method of Space Membrane Deployable Mechanism

Based on the data-driven framework developed by Bessa [38], the response surface (RS) method is adopted to establish the surrogate model of the space membrane deployable mechanism for its dynamic characteristics and to conduct multiobjective design, as illustrated in Figure 11.

4.1. Sample Points

On the basis of the numerical analysis in the previous section, the sample points are obtained according to the design of experiments (DoE). The response of the dynamic property of the membrane mechanism $\tilde{y}(x)$ can be represented by the polynomial:

$$\tilde{y}(x) = \sum_{i=1}^{n} \beta_i \varphi_i(x) \tag{22}$$

in which n and β_i represent the number and coefficients of basis functions φ_i, and i represents the design variable number. According to the comprehensive analysis of the computational accuracy and efficiency, the quartic polynomials are used for the basis functions, as shown in Equation (23):

$$\begin{array}{l} 1, x_1, x_2, \ldots, x_n \\ x_1^2, x_1 x_2, \ldots, x_1 x_n, \ldots, x_n^2 \\ x_1^3, x_1^2 x_2, \ldots, x_1^2 x_n, x_1 x_2^2, \ldots, x_1 x_n^2, \ldots, x_n^3 \\ x_1^4, x_1^3 x_2, \ldots, x_1 x_n^3, x_1^2 x_2^2, \ldots, x_1^2 x_n^2, \ldots, x_1 x_2^3, \ldots, x_1 x_n^3, \ldots, x_n^4 \end{array} \tag{23}$$

According to the above parametric studies in this paper, cable tension F and membrane thickness t are selected as design variables to conduct subsequent analysis. As shown in Table 4, cable tension F varies from 30 N to 40 N, referring to the design experience of a typical space membrane mechanism, and membrane thickness t varies from 25 μm to 125 μm, according to the actual thickness of Kapton. Then, five-level DoE is adopted to obtain 25 sample points with the ω_{FE} results based on the numerical analysis.

Table 4. FE results of the sample points.

No.	*F* (N)	*t* (μm)	ω_{FE} (Hz)
1	30	25	0.13015
2	30	50	0.09243
3	30	75	0.07561
4	30	100	0.06553
5	30	125	0.05863
6	32.5	25	0.13509
7	32.5	50	0.09597
8	32.5	75	0.07849
9	32.5	100	0.06803
10	32.5	125	0.06087
11	35	25	0.13983
12	35	50	0.09935
13	35	75	0.08126
14	35	100	0.07043
15	35	125	0.06301
16	37.5	25	0.14438
17	37.5	50	0.10259
18	37.5	75	0.08392
19	37.5	100	0.07273
20	37.5	125	0.06507
21	40	25	0.14875
22	40	50	0.10572
23	40	75	0.08648
24	40	100	0.07495
25	40	125	0.06705

4.2. Surrogate Model

According to the least-square method, coefficients of the basic functions $b = (\beta_1, \beta_2 \cdots \beta_n)$ can be obtained as follows:

$$b = \left(\boldsymbol{\Phi}^T \boldsymbol{\Phi}\right)^{-1} \left(\boldsymbol{\Phi}^T y\right) \tag{24}$$

where matrix $\boldsymbol{\Phi}$ is

$$\boldsymbol{\Phi} = \begin{bmatrix} \varphi_1(l,w)_1 & \cdots & \varphi_N(l,w)_1 \\ \vdots & \ddots & \vdots \\ \varphi_1(l,w)_M & \cdots & \varphi_N(l,w)_M \end{bmatrix} \tag{25}$$

in which M represents the number of sample points. Based on Equations (22)–(25), the surrogate model can be established by substituting the sample points. Consequently, ω is derived as follows:

$$\begin{aligned} \omega = {} & 0.106699 - 0.00312t + 0.004087F \\ & + 5.31415 \times 10^{-5} t^2 - 6.35411 \times 10^{-5} Ft \\ & - 7.33 \times 10^{-6} F^2 - 4.17 \times 10^{-7} t^3 \\ & + 4.72 \times 10^{-7} t^2 F + 2.93 \times 10^{-7} t F^2 \\ & - 4.21 \times 10^{-7} F^3 + 1.20 \times 10^{-9} t^4 \\ & - 1.30 \times 10^{-9} t^3 F - 9.67 \times 10^{-10} F^2 t^2 \\ & - 6.40 \times 10^{-10} t F^3 + 4.27 \times 10^{-9} F^4 \end{aligned} \tag{26}$$

In order to assess the accuracy of Equation (26), several criteria need to be calculated, including relative error *RE*, coefficient of multiple determination R^2, adjusted coefficient of the multiple determination ${R^2}_{adj}$ and root mean square error *RMSE*.

$$RE = \frac{\tilde{y}_i - y_i}{y_i} \tag{27}$$

$$R^2 = 1 - \frac{SSE}{SST} \tag{28}$$

$$R^2_{adj} = 1 - \frac{M-1}{M-N}\left(1 - R^2\right) \tag{29}$$

$$RMSE = \left(\frac{SSE}{M-N-1}\right)^{0.5} \tag{30}$$

in which y_i represents $\omega_{\rm FE}$, SST is the total sum of the squares $SST = \sum_{i=1}^{M}(y_i - \bar{y})^2$ and SSE the sum of squared estimate of errors $SSE = \sum_{i=1}^{M}(y_i - \tilde{y})^2$.

As shown in Table 5, $\omega_{\rm FE}$ and $\omega_{\rm RS}$ are compared and then substituted into the Equations (27)–(30) to calculate the assessment criteria. As listed in Table 6, the REs are less than 0.08%, and R^2 and $R^2{}_{adj}$ are close to 1, indicating that Equation (26) can be applied to calculate the fundamental frequency of the membrane mechanism. Thus, the response surface of the dynamic characteristic for the membrane mechanism is plotted in Figure 12.

Table 5. Comparison between $\omega_{\rm FE}$ and $\omega_{\rm RS}$.

No.	$\omega_{\rm FE}$ (Hz)	$\omega_{\rm RS}$ (Hz)	RE (%)
1	0.13015	0.13016	0.0077
2	0.09243	0.09239	−0.0433
3	0.07561	0.07567	0.0794
4	0.06553	0.06549	−0.0610
5	0.05863	0.05864	0.0171
6	0.13509	0.13510	0.0074
7	0.09597	0.09595	−0.0208
8	0.07849	0.07852	0.0382
9	0.06803	0.06801	−0.0293
10	0.06087	0.06087	0.0016
11	0.13983	0.13983	−0.0009
12	0.09935	0.09935	0.0030
13	0.08126	0.08126	0.0004
14	0.07043	0.07042	−0.0142
15	0.06301	0.06301	0.0067
16	0.14438	0.14437	−0.0069
17	0.10259	0.10262	0.0292
18	0.08392	0.08389	−0.0357
19	0.07273	0.07275	0.0275
20	0.06507	0.06507	−0.0075
21	0.14875	0.14874	−0.0067
22	0.10572	0.10576	0.0378
23	0.08648	0.08642	−0.0694
24	0.07495	0.07500	0.0667
25	0.06705	0.06704	−0.0149

Table 6. Accuracy of the RS model for the membrane mechanism.

Option	Value
R^2	0.999999
$R^2{}_{adj}$	0.999998
$RMSE$	4.54996×10^{-5}
RE	[−0.0694% 0.0794%]

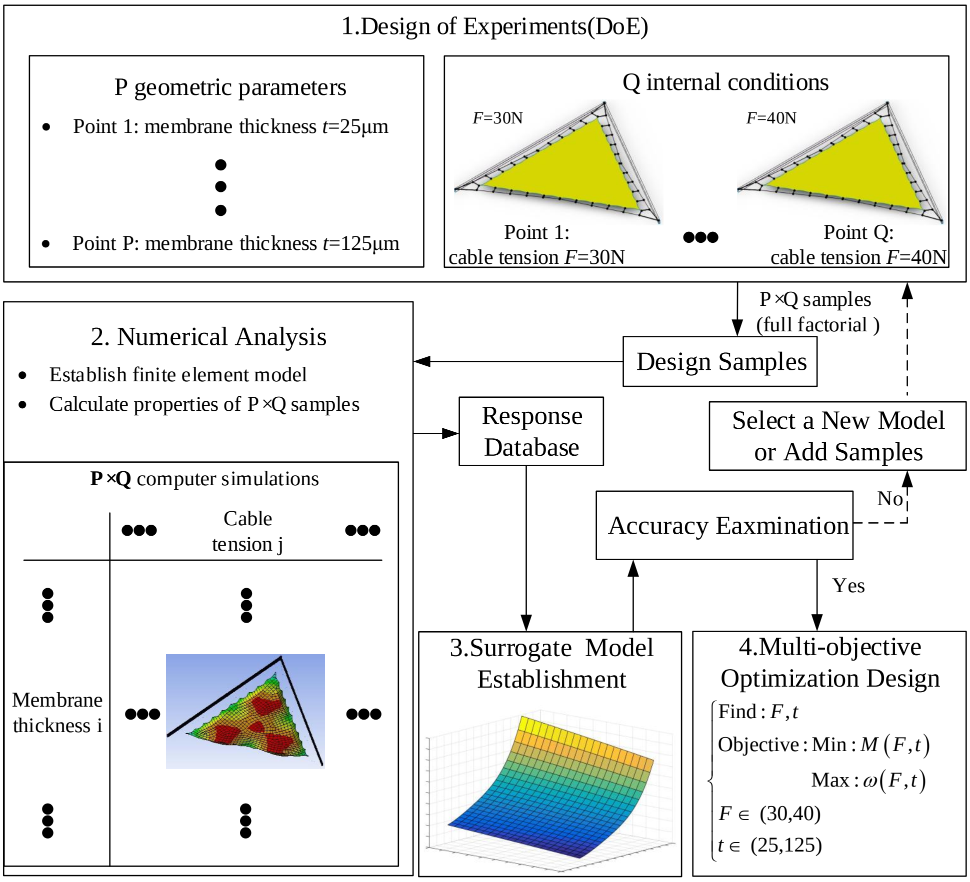

Figure 11. RS method applied to the design of space membrane deployable mechanism.

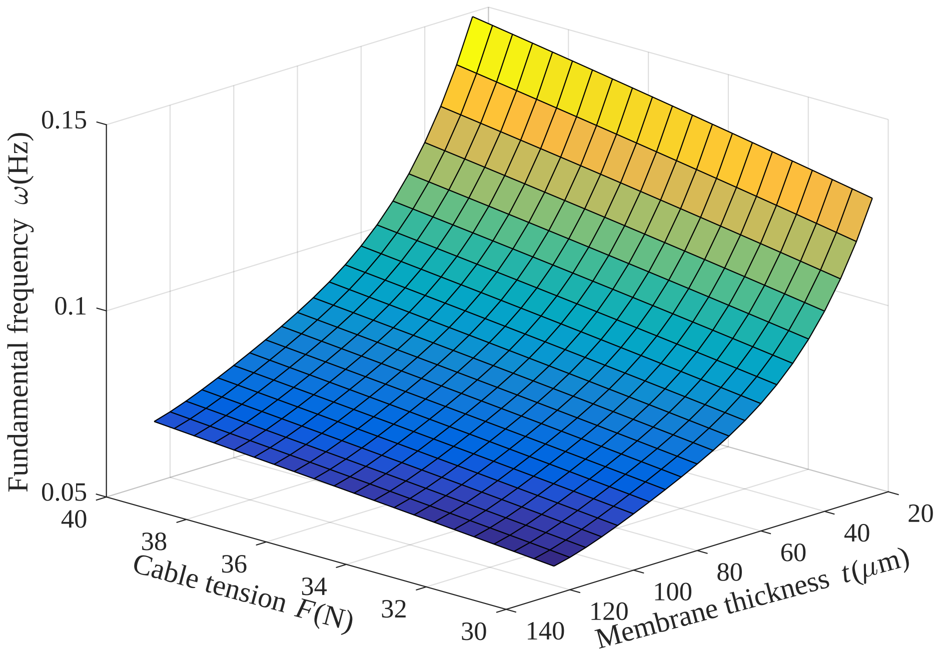

Figure 12. Response surface of the dynamic characteristic for the membrane mechanism.

4.3. Multiobjective Optimization Design

Combined with the above research results, multiobjective optimization design for the membrane mechanism is conducted based on the genetic algorithm to obtain the optimal dynamic and lightweight design parameters. According to the analysis in previous sections, the design parameters cable tension F and membrane thickness t possess a pronounced effect on the fundamental frequency ω and total mass M, which are taken as the objective functions, as derived in Equation (31).

$$\begin{cases} \text{Max}: \omega = 0.106699 - 0.00312t + 0.004087F \\ + 5.31415 \times 10^{-5}t^2 - 6.35411 \times 10^{-5}Ft \\ - 7.33 \times 10^{-6}F^2 - 4.17 \times 10^{-7}t^3 \\ + 4.72 \times 10^{-7}t^2F + 2.93 \times 10^{-7}tF^2 \\ - 4.21 \times 10^{-7}F^3 + 1.20 \times 10^{-9}t^4 \\ - 1.30 \times 10^{-9}t^3F - 9.67 \times 10^{-10}F^2t^2 \\ - 6.40 \times 10^{-10}tF^3 + 4.27 \times 10^{-9}F^4 \\ \text{Min}: M = 0.0013F + 0.388t + 32.54 \\ F \in (30, 40) \\ t \in (25, 125) \end{cases} \tag{31}$$

As for the settlements of the genetic algorithm, the uniform crossover and random selection type are adopted with a population size of 400 and a crossover rate of 0.9. When the variation rate is adjusted to 0.5, the multiobjective optimization design parameters and the local optimal solution in a given range are obtained, and the convergence of the genetic algorithm is computed by the convergence curve. As listed in Table 7, the optimal membrane mechanism parameters are F = 40 N and t = 25 μm, resulting in the membrane mechanism with the highest stiffness of ω = 0.1487 Hz and the lowest mass of M = 42.292 kg. From Figure 12 and the mass equation, the same results can be obtained, which also verifies the correctness of the optimization calculation. However, when the configuration is changed, or there are other parameters and variables with unobvious, nonmonotonic relationships, the method based on the monotonicity of figures and equations would be invalid. However, the multiobjective optimization based on the genetic algorithm in this section can provide guidance, including the multiobjective modeling method and solution algorithm.

The multiobjective optimization here provides solutions to obtain the optimal dynamic and lightweight design parameters, laying the foundation for the research and development of the boom–cable–membrane mechanism to be widely utilized in space missions. In addition, the surrogate model and multiobjective optimization proposed can be applied to other performance indices such as surface accuracy or more complex structure by presenting a general analytical framework, which warrants further study in subsequent research.

Table 7. Multiobjective optimization result for the membrane mechanism.

Type	Option	Value
Design parameter	F (N)	40
Design parameter	t (μm)	25
Objective result	ω (Hz)	0.1487
Objective result	M (kg)	42.292

5. Conclusions

According to the property requirements of space deployable structures, this paper proposes the triangular space membrane deployable mechanism based on deployable booms with lightweight, high deployment ratio, high stiffness and large size. These features are primarily generated by the STEM deployable booms and web-like tensioned membrane scheme, the mechanical property and total mass of which are analyzed and deduced, respectively. Then, the membrane mechanism simulation model, including booms, cables and membrane, is built and verified by the membrane model test, which aims to reveal the relationship between its fundamental frequency and design parameters. The dynamic surrogate model of the design variables in respect to the fundamental frequency of the membrane mechanism is created through the response surface approach. Additionally, based on the genetic algorithm, a comprehensive multiobjective optimization to achieve high stiffness and minimal mass is performed to obtain the optimal dynamic and lightweight design parameters of the membrane mechanism.

This study endorses the exploitation of mass derivation and the mathematical surrogate model to set up a theoretical analysis basis for the membrane mechanism. On the other hand, the configuration design process and the multiobjective optimization modeling presented in this paper pave the way to design a more novel space membrane deployable mechanism with exhilarating features and properties.

Author Contributions: Conceptualization, Y.T., H.G., Z.W. and R.L.; methodology, Y.T.; software, Y.T.; validation, Y.T., W.Z. and C.X.; formal analysis, Y.T.; investigation, Y.T., W.Z. and C.X.; data curation, Y.T.; writing—original draft preparation, Y.T.; writing—review and editing, H.G. and R.L.; visualization, Y.T.; supervision, H.G. and R.L.; project administration,Z.W. and R.L. All authors have read and agreed to the published version of the manuscript.

Funding: The authors would like to acknowledge that the research presented in this paper was carried out with the aid of the National Natural Science Foundations of China (51835002) and Open Project of Space Structure and Mechanism Technology Laboratory of China Aerospace Science and Technology Group Co., Ltd. (YYHT-F805201904004). The support provided by China Scholarship Council (CSC) during a visit of Yuzhen Tang to University of Nottingham is acknowledged.

Institutional Review Board Statement: Not applicable.

Informed Consent Statement: Not applicable.

Data Availability Statement: Not applicable.

Conflicts of Interest: The authors declare no conflict of interest.

References

1. Pellegrino, S. *Deployable Structures*; Springer: Vienna, Austria, 2001.
2. Chandra, M.; Kumar, S.; Chattopadhyaya, S.; Chatterjee, S.; Kumar, P. A review on developments of deployable membrane-based reflector antennas. *Adv. Space Res.* **2021**, *68*, 3749–3764. [CrossRef]
3. Liu, Z.Q.; Hui, Q.; Xiao, L.; Yang, S.L. Review of Large Spacecraft Deployable Membrane Antenna Structures. *Chin. J. Mech. Eng.* **2017**, *30*, 1447–1459. [CrossRef]
4. Fang, H.; Knarr, K.; Quijano, U.; Huang, J.; Thomson, M. In-space deployable reflectarray antenna: Current and future. In Proceedings of the 49th AIAA/ASME/ASCE/AHS/ASC Structures, Structural Dynamics, and Materials Conference, 16th AIAA/ASME/AHS Adaptive Structures Conference, 10th AIAA Non-Deterministic Approaches Conference, 9th AIAA Gossamer Spacecraft Forum, 4th AIAA Multidisciplinary Design Optimization Specialists Conference, Schaumburg, IL, USA, 7–10 April 2008; p. 2209.
5. Chodimella, S.; Moore, J.; Otto, J.; Fang, H. Design evaluation of a large aperture deployable antenna. In Proceedings of the 47th AIAA/ASME/ASCE/AHS/ASC Structures, Structural Dynamics, and Materials Conference, Newport, RI, USA, 1–4 May 2006; p. 1603.
6. Soma, E.; Endo, T.; Tanaka, K.; Miyauchi, M.; Yokota, R.; Tsuda, Y.; Mori, O.; Ikaros, D.T. Flexible Solar Array of Small Solar Power Sail Demonstrator "IKAROS". *Trans. Jpn. Soc. Aeronaut. Space Sci. Aerosp. Technol. Jpn.* **2012**, *10*, Po_4_27–Po_4_31. [CrossRef]
7. Liu, X.; Lv, L.; Cai, G. Active nonlinear vibration control of a membrane solar array structure. *Proc. Inst. Mech. Eng. Part G J. Aerosp. Eng.* **2022**, *236*, 3186–3200. [CrossRef]
8. Gong, S.; Macdonald, M. Review on solar sail technology. *Astrodynamics* **2019**, *3*, 93–125. [CrossRef]
9. Johnson, L.; Young, R.M.; Montgomery IV, E.E. Recent advances in solar sail propulsion systems at NASA. *Acta Astronaut.* **2007**, *61*, 376–382. [CrossRef]
10. Wilkie, W.K. Overview of the NASA Advanced Composite Solar Sail System (ACS3) Technology Demonstration Project. In *AIAA Scitech 2021 Forum*; AIAA: Sterling, VA, USA, 2021 .
11. Lane, S.A.; Murphey, T.W.; Zatman, M. Overview of the Innovative Space-Based Radar Antenna Technology Program. *J. Spacecr. Rocket.* **2011**, *48*, 135–145. [CrossRef]

12. Straubel, M.; Block, J.; Sinapius, M.; Hühne, C. Deployable composite booms for various gossamer space structures. In Proceedings of the 52nd AIAA/ASME/ASCE/AHS/ASC Structures, Structural Dynamics and Materials Conference, Denver, CO, USA, 4–7 April 2011; p. 2023.
13. NASA. Hubble Space Telescope Reaches Orbit. 2014. Available online: https://www.nasa.gov/content/hubble-space-telescope-reaches-orbit (accessed on 6 October 2022).
14. Delleur, A.; Kerslake, T. Managing ISS US Solar Array Electrical Hazards for SSU Replacement via EVA. In Proceedings of the 2nd International Energy Conversion Engineering Conference, Providence, RI, USA, 16–19 August 2004; p. 5500.
15. Pedivellano, A.; Pellegrino, S. Deployment Dynamics of Thin-Shell Space Structures. *J. Spacecr. Rocket.* **2022**, *59*, 1214–1227. [CrossRef]
16. Hoang, B.; White, S.; Spence, B.; Kiefer, S. Commercialization of Deployable Space Systems' roll-out solar array (ROSA) technology for Space Systems Loral (SSL) solar arrays. In Proceedings of the 2016 IEEE Aerospace Conference, Big Sky, MO, USA, 5–12 March 2016; pp. 1–12.
17. Sawada, H.; Mori, O.; Okuizumi, N.; Shirasawa, Y.; Miyazaki, Y.; Natori, M.; Matunaga, S.; Furuya, H.; Sakamoto, H. Mission report on the solar power sail deployment demonstration of IKAROS. In Proceedings of the 52nd AIAA/ASME/ASCE/AHS/ASC Structures, Structural Dynamics and Materials Conference, Denver, CO, USA, 4–7 April 2011; p. 1887.
18. Heaton, A.F.; Faller, B.F.; Katan, C.K. NanoSail: D orbital and attitude dynamics. In *Advances in Solar Sailing*; Springer: Berlin/Heidelberg, Germany, 2014; pp. 95–113.
19. Chmielewski, A.; Jenkins, C. Gossamer spacecraft. In *WIT Transactions on State-of-the-art in Science and Engineering*; WIT Press: Southampton, UK, 2005; Volume 20.
20. Ruggiero, E.J.; Inman, D.J. Gossamer Spacecraft: Recent Trends in Design, Analysis, Experimentation, and Control. *J. Spacecr. Rocket.* **2006**, *43*, 10–24. [CrossRef]
21. Jenkins, C.; Korde, U.A. Membrane vibration experiments: An historical review and recent results. *J. Sound Vib.* **2006**, *295*, 602–613. [CrossRef]
22. Shen, Y.; Zheng, W.; Wang, X. Dynamic and vibration analysis of a SAR membrane antenna. In Proceedings of the ASME International Mechanical Engineering Congress and Exposition, Seattle, WA, USA, 11–15 November 2007; Volume 42959, pp. 17–24.
23. Liu, X.; Cai, G.P.; Peng, F.J.; Zhang, H.; Lv, L.L. Nonlinear vibration analysis of a membrane based on large deflection theory. *J. Vib. Control* **2018**, *24*, 2418–2429. [CrossRef]
24. Liu, X.; Zhang, H.; Lv, L.; Peng, F.; Cai, G. Vibration control of a membrane antenna structure using cable actuators. *J. Frankl. Inst.* **2018**, *355*, 2424–2435. [CrossRef]
25. Fan, L.; Liu, X.; Cai, G.P. Dynamic modeling and modal parameters identification of satellite with large-scale membrane antenna. *Adv. Space Res.* **2019**, *63*, 4046–4057. [CrossRef]
26. Ahmadi, M.; Hashemi, G.; Jamali, M.; Dehkordi, M.R.; Razavian, S.A. Nonlinear free vibration analysis of pre-stressed membranes. *Proc. Inst. Mech. Eng. Part K J. Multi-Body Dyn.* **2017**, *231*, 346–356. [CrossRef]
27. Zhang, Y.; Hiruta, T.; Kajiwara, I.; Hosoya, N. Active vibration suppression of membrane structures and evaluation with a non-contact laser excitation vibration test. *J. Vib. Control* **2017**, *23*, 1681–1692. [CrossRef]
28. Chakravarty, U.K.; Albertani, R. Experimental and Finite Element Modal Analysis of a Pliant Elastic Membrane for Micro Air Vehicles Applications. *J. Appl. Mech.* **2012**, *79*, 021004. [CrossRef]
29. Cammarata, A.; Sinatra, R.; Rigato, R.; Maddio, P.D. Tie-System Calibration for the Experimental Setup of Large Deployable Reflectors. *Machines* **2019**, *7*, 23. [CrossRef]
30. Lima-Rodriguez, A.; Garcia-Manrique, J.; Dong, W.; Gonzalez-Herrera, A. A Novel Methodology to Obtain the Mechanical Properties of Membranes by Means of Dynamic Tests. *Membranes* **2022**, *12*, 288. [CrossRef]
31. Gaspar, J.L.; Solter, M.J.; Pappa, R.S. Membrane vibration studies using a scanning laser vibrometer. In Proceedings of the 20th International Modal Analysis Conference, Los Angeles, CA, USA, 4–7 February 2002.
32. Leipold, M.; Runge, H.; Sickinger, C. Large SAR membrane antennas with lightweight deployable booms. In Proceedings of the 28th ESA Antenna Workshop on Space Antenna Systems and Technologies, ESA/ESTEC, Noordwijk, The Netherlands, 31 May–3 June 2005; Volume 6.
33. Natori, M.; Katsumata, N.; Okuizumi, N.; Watanabe, A.; Yamakawa, H. Deployable Membrane Structures with Rolled-up Booms and Their Deployment Characteristics. In Proceedings of the 54th AIAA/ASME/ASCE/AHS/ASC Structures, Structural Dynamics, and Materials Conference, Boston, MA, USA, 8–11 April 2013; p. 1596.
34. Okuizumi, N.; Katsumata, N.; Natori, M.C.; Yamakawa, H. Stepwise Deployment of Membrane Space Structures with Rolled-up Booms: Experiments and Simulations. In Proceedings of the Spacecraft Structures Conference, National Harbor, MD, USA, 13–17 January 2014.
35. Ikeya, K.; Sakamoto, H.; Nakanishi, H.; Furuya, H.; Tomura, T.; Ide, R.; Iijima, R.; Iwasaki, Y.; Ohno, K.; Omoto, K.; et al. Significance of 3U CubeSat OrigamiSat-1 for space demonstration of multifunctional deployable membrane. *Acta Astronaut.* **2020**, *173*, 363–377. [CrossRef]
36. Acar, P.; Nikbay, M.; Aslan, A.R. Design Optimization of a 3-Unit Satellite De-Orbiting Mechanism. In Proceedings of the ESA Small Satellites Systems and Services the 4S Symposium, Portoroz, Slovenia, 4–8 June 2012; pp. 4–8.

37. Liu, X.; Cai, G.; Peng, F.; Zhang, H. Dynamic model and active vibration control of a membrane antenna structure. *J. Vib. Control* **2018**, *24*, 4282–4296. [CrossRef]
38. Bessa, M.A.; Pellegrino, S. Design of ultra-thin shell structures in the stochastic post-buckling range using Bayesian machine learning and optimization. *Int. J. Solids Struct.* **2018**, *139–140*, 174–188. [CrossRef]